Substructure of Visibility Functions from Scattered Radio Emission of Pulsars through Space VLBI

M. V. Popov[1] ⓘ, N. Bartel[2], M. S. Burgin[1] ⓘ, C. R. Gwinn[3] ⓘ, T. V. Smirnova[4], and V. A. Soglasnov[1]
[1] Lebedev Physical Institute, Astro Space Center, Profsoyuznaya 84/32, Moscow, 117997, Russia; mburgin@asc.rssi.ru
[2] York University, 4700 Keele Street, Toronto, ON M3J 1P3, Canada
[3] University of California at Santa Barbara, Santa Barbara, CA 93106-4030, USA
[4] Lebedev Physical Institute, Pushchino Radio Astronomy Observatory, Pushchino 142290, Moscow region, Russia

Abstract

We report on the substructure of visibility functions in the delay domain of PSRs B0329+54, B0823+26, B0834 +06, B1933+16, and B0833–45 (Vela) observed with Earth–Earth and *RadioAstron* space–Earth two-element interferometers at frequencies of 324 and 1668 MHz. All visibility functions display unresolved spikes distributed over a range of delays. They are due to band-limited scintillation noise and related to the scattering time. The envelopes for each but the Vela pulsar are well fit by a single Lorentzian, which we interpret as being indicative of isotropic scattering on the plane of the sky due to a thin scattering screen between the pulsar and us. In contrast, the envelope for the Vela pulsar needs to be mostly fit by at least two Lorentzians, a narrow and a broad one at the same zero delay. We interpret this characteristic as indicative of anisotropic scattering due to a more complex structure of scattering screens in the supernova remnant. The possibility of describing the delay visibility functions by Lorentzians is likely a general property of pulsars and offers a new way of describing the scattering parameters of the intervening interstellar medium. Furthermore, for all of our pulsars, the unresolved spikes in visibility functions of similar projected baselines were well correlated, indicating that the telescopes are located in the same diffraction spot. The correlation vanished for visibilities from largely different baselines, when some radio telescopes are not in the same spot.

1. Introduction

Radio emission of compact celestial radio sources in our Galaxy and beyond can be strongly scattered by inhomogeneities of the interstellar medium (ISM) located between the source and the observer. This process causes angular broadening of the source image, distortion of radio spectra, and intensity fluctuations or scintillations of the radio emission (see, e.g., Prokhorov et al. 1975; Rickett 1977; Gwinn et al. 1998; Shishov et al. 2003). Here we focus on the effects of scattering on very long baseline interferometry (VLBI) and space VLBI observations of compact sources at frequencies at which these effects are strong. We have chosen pulsars as targets, since they are intrinsically pointlike even when observed with space VLBI on baselines as long as 200,000 km, as provided by *RadioAstron* (Kardashev et al. 2013). Therefore, the structure of the source does not need to be considered in the analysis, and the results are essentially exclusively due to scattering characteristics of the ISM (see, e.g., Johnson & Gwinn 2015; Johnson 2016; Johnson & Narayan 2016 for recent studies on this subject). In previous studies, some characteristics of the scattering screens in the ISM in terms of the pulsar's scintillation time, t_{scint}; scattering time, τ_{sc}; angular size of the scattering disk, θ_{sc}; and decorrelation bandwidth, Δf_{dif}, were already obtained. Assuming a single thin scattering screen and combining τ_{sc} with θ_{sc}, the distance, d_s, of the scattering screen relative to the distance, D, of the pulsar could be determined. An analysis of these measurements indicates a possible layered structure of the interstellar plasma in our Galaxy (Gwinn et al. 2016; Popov et al. 2016, 2017, 2019; Fadeev et al. 2018). In previous work, Popov et al. (2016) presented an example of the

VLBI visibility function for the pulsar PSR B1749–28. They found for the first time that for this pulsar, the dependence of the average visibility function on delay can be well fit by a Lorentzian. In this paper, we follow Popov et al. (2016) and focus on five more pulsars, four of them older pulsars and one of them the young Vela pulsar, PSR B0833–45, which is still embedded in its supernova remnant and also likely in the larger Gum Nebula. We selected the pulsars on the basis of their peak flux density in order to get a sufficiently high signal-to-noise ratio for the analysis, as well as on the basis of the selected pulsars having a relatively large range of dispersion measures. Further, the scattering time, τ_{sc}, needed to be large enough so that a sufficiently large number of points of the envelope could be used for the model fit. Since the bandwidth of our VLBI and space VLBI observations was 16 MHz, the sampling step in delay of our visibility functions was 31.25 ns. That restricted our choice to pulsars with $\tau_{sc} \gtrsim 0.5\ \mu$s so that at least a dozen sampling points could be used for the fit. An additional concern was the selection of the observing frequency. Usually, our first choice was to use data obtained at the lowest of the available frequencies, namely 324 MHz. However, for two pulsars, the dispersion measure was so high that we needed to select the next higher available frequency, namely 1668 MHz, to allow for a good fit of the visibility function.

Table 1 lists the pulsars with their periods, dispersion measures, distances, galactic coordinates, observing frequencies, scattering parameters obtained at the observing frequencies, and ratios of the distance of the scattering screen relative to the distance of the pulsar, obtained in our previous publications cited above. This is a small but somewhat

Table 1
Parameters of Pulsars

PSR	P (s)	DM (pc cm^{-3})	D (kpc)	l (deg)	b (deg)	ν (MHz)	t_{scint} (s)	τ_{sc} (μs)	θ_{sc} (mas)	Δf_{dif} (kHz)	d_s/D	Reference
(1)	(2)	(3)	(4)	(5)	(6)	(7)	(8)	(9)	(10)	(11)	(12)	(13)
B0329+54	0.714	26.7	1.03	145.0	−1.2	324	110	4.1	4.8	7.0	0.60	1
B0823+26	0.531	19.4	0.36	197.0	31.7	324	70	0.46	1.8	140	0.72	2
B0834+06	1.274	12.8	0.62	219.7	26.3	324	220	0.69	1.2	210	0.64	2
B1933+16	0.359	158.5	3.70	52.4	−2.1	1668	42	0.85	0.84	50	0.73	3
B0833−45	0.089	69.0	0.29	263.6	−2.8	1668	6.2	7.6	6.4	7.3	0.79-0.87	4

Note. Columns are as follows: (1) pulsar name, (2) pulsar period, (3) dispersion measure, (4) distance, (5) galactic longitude, (6) galactic latitude, (7) observing frequency, (8) scintillation time, (9) scattering time, (10) scattering angle, (11) decorrelation bandwidth, (12) ratio of the distance of the scattering screen to the distance of the pulsar, and (13) reference where the parameters in columns (10)–(12) were determined.
References. (1) Popov et al. (2017), (2) Fadeev et al. (2018), (3) Popov et al. (2016), (4) Popov et al. (2019).

Table 2
Parameters of Data Reduction

PSR	Obs. Code	Date (yy.mm.dd)	ν (MHz)	T_{scan} (s)	T_{tot} (hr)	Pol.	N_{ch}	δt_{cor} (s)	T_{vis} (s)	Radio Telescopes
(1)	(2)	(3)	(4)	(5)	(6)	(7)	(8)	(9)	(10)	(11)
B0329+54	RAES10,a-d	2012 Nov 26–29	324	570	4	LR	4096	0.714	34.3	GB
B0823+26	RAGS04ak,aj	2014 Mar 11	324	1170	17	LR	1024	0.5306	34.0	GB,WB
B0834+06	RAGS04al	2015 Apr 8	324	1170	1.5	LR	65536	1.2737	145.2	AR,GB,WB
B1933+16	RAKS02aa	2013 Aug 1	1668	570	1.5	R	2048	0.3587	31.6	AR,TR,SV
B0833−45	RAKS02as	2013 Dec 15	1668	1170	2.5	LR	8192	0.9830	7.9	AT,HO,CD,HH
B0833−45	RAES07a	2012 May 10	1668	570	3.0	LR	8192	0.9830	7.9	PA,MP,TI,HH,HO
B0833−45	RAES07b	2012 May 18	1668	570	1.5	LR	8192	0.9830	7.9	PA,AT,HO,MP,HH

Note. Columns are as follows: (1) pulsar name, (2) code of the experiment, (3) date of observation, (4) observing center frequency, (5) duration of observing scan in seconds, (6) total observing time in hours, (7) circular polarization, left hand, LCP, L, right hand, RCP, R, (8) number of channels used in the correlator, (9) sampling time of the correlator output in seconds, (10) time in seconds for visibility calculation, (11) Earth radio telescopes: AR—Arecibo, GB—Green Bank, AT—Australia Telescope Compact Array, HO—Hobart, HH—Hartebeesthoek, CD—Ceduna, MP—Mopra, SV—Svetloye, TI—Tidbinbilla, PA—Parkes, WB—Westerbork.

representative list of pulsars with respect to the range of dispersion measures, galactic latitudes, and scattering times.

Of particular interest in our work reported here are investigations of the influence of scattering on the interferometric visibility function of a two-element interferometer. The detailed analysis of the substructure of the visibility function may give us additional information on the characteristics of the scattering screens. Early theoretical studies of visibility functions of two-element interferometers were presented by Goodman & Narayan (1989) and Narayan & Goodman (1989). They distinguished between fast and slow refractive scintillations with corresponding timescales of t_{dif} and t_{ref}, with the diffractive timescale in particular related to the size of the diffraction spot, ρ_{dif}. The physical interpretation of a visibility function depends on the integration time, t_{int}, and its relation to the two timescales. We can distinguish between the snapshot mode when $t_{int} < t_{dif}$, averaged mode when $t_{dif} < t_{int} < t_{ref}$, and ensemble averaging mode when $t_{int} > t_{ref}$. For the meter and decimeter wavelength range typical timescales, t_{dif} and t_{ref}, sources in our Galaxy are several minutes for diffraction scintillations and several weeks for refraction scintillations, respectively. For our VLBI observations with typical scan lengths of 1000 s, the visibility function can be measured in either the snapshot mode or the averaged mode. Here we present an analysis of the structure of the delay visibility function for our pulsars in the snapshot and average modes and search for characteristics that can be related to scattering properties.

2. Observations and Data Reduction

Our observations were carried out as part of the scientific program of the *RadioAstron* space VLBI mission (Kardashev et al. 2013). For this study, we selected pulsar data from several projects: RAES07a, RAES07b, and RAES10a-d, related to the *RadioAstron* Early Science Program; RAGS04aj, RAGS04ak, and RAGS04al, related to general observing time proposals; and RAKS02aa and RAKS02as, related to the Key Science Program. The observation and data reduction parameters are given in Table 2.

All of our data were processed with the ASC correlator in Moscow with gating and dedispersion activated (Likhachev et al. 2017). The ON-pulse window was centered on the main component of the average profile, and the OFF-pulse window was offset from the main pulse by half a period and had the same width as the ON-pulse window. The OFF-pulse window was used to establish bandpass correction for auto- and cross-spectra. The correlator output was sampled synchronously with the pulsar period. The results of the correlation were given as complex cross-correlation spectra (cross-spectra) written in standard FITS format. In general, the cross-spectra were obtained for each period of the pulsar. Only for pulsar B0833–45 (Vela) with a very short period (0.0892 s) were cross-spectra integrated in the correlator over 10 periods, still providing good time resolution for further analysis.

At the next stage, we retrieved the results of correlation processing from the FITS files using the CFITSIO package (Pence 1999) and computed the fringe visibility magnitude

$|V_{A-B}(\tau, f)|$ as a function of delay, τ, and fringe rate, f, for every time interval of duration T_{vis} with $T_{vis} < t_{scint}$ by using the $T_{vis}/\delta t_{cor}$ consequent complex cross-spectra from the correlator output for each two-element interferometer with stations A and B. Then, for each τ, we determined the fringe rate that maximizes $|V_{A-B}(\tau, f)|$. Not surprisingly, these fringe rates were always close to zero. For further analysis, we used the cross section, $|V_{A-B}(\tau, f_{max})| = |V_{A-B}(\tau)|$ at f_{max}. For every scan of duration T_{scan}, we obtained T_{scan}/T_{vis} cross sections of the visibility function, $|V_{A-B}(\tau)|$. We call this set of cross sections of the visibility magnitudes, which are consecutive in time, t, the dynamic visibility magnitude, $|DV_{A-B}(\tau, t)|$.

Our goal was to probe these functions in detail, study their characteristics as a function of projected baseline length (where possible), and extract scintillation parameters from them. Since these functions were relatively noisy and not appropriate for obtaining single scintillation parameter values, we used two-dimensional cross-correlation functions (CCFs) and autocorrelation functions (ACFs) to improve the signal-to-noise ratio.

We distinguish between one- and two-baseline correlations of interferometer observations. In particular, for one-baseline correlations of interferometer observations, we compute the two-dimensional CCFs $2dCCF^{LR}(\Delta\tau, \Delta t)$ between the left-circular polarization (LCP) and right-circular polarization (RCP) channels of $|DV_{A-B}(\tau, t)|$. First, we subtracted the mean level in every $|DV_{A-B}(\tau, t)|$ determined "off-spot," i.e., outside the region of increased values of $|V_{A-B}(\tau)|$. Then we computed the CCFs.[5] The resulting functions, $2dCCF^{LR}(\Delta\tau, \Delta t)$, were then normalized by the corresponding 2dACF, that is, by

$$\sqrt{2dACF^L(\Delta\tau = 0, \Delta t = 0) \times 2dACF^R(\Delta\tau = 0, \Delta t = 0)}.$$

For the observations of B1933+16 and part of those of PSR B0833−45 (Vela), we recorded only LCP or RCP and therefore considered only the ACFs, $2dACF^L(\Delta\tau, \Delta t)$ or $2dACF^R(\Delta\tau, \Delta t)$, for our further analysis of one-baseline correlations, instead of the CCF between the RCP and LCP channels.

The last functions to mention concern two-baseline correlations of interferometer observations. Here we measure similarities between the output of, for instance, a short baseline interferometer and a long baseline interferometer to obtain information about the difference in the diffraction pattern the two interferometers observe. The resulting functions are $2dCCF^{LL}_{(A-B)\times(C-D)}$ and $2dCCF^{RR}_{(A-B)\times(C-D)}$, which are the cross-correlations between $|DV^L_{A-B}(\tau, t)|$ and $|DV^L_{C-D}(\tau, t)|$ for the two baselines, AB and CD, for the LCP channel and the equivalent correlations for the RCP channel. At the heart of our analysis are the cross sections of these functions at $\Delta t = 0$. These are the one-dimensional functions $CCF^{LR}_{A-B}(\Delta\tau)$, $ACF^L_{A-B}(\Delta\tau)$, $ACF^R_{A-B}(\Delta\tau)$, $CCF^L_{(A-B)\times(C-D)}(\Delta\tau)$, and $CCF^R_{(A-B)\times(C-D)}(\Delta\tau)$.

---

[5] For technical reasons, instead of cross-correlating the two functions directly, we derived the cross-correlation by using the cross-correlation theorem. This procedure simplified the computation in our case. We computed the functions 2dCCF as the inverse Fourier transform of the product of the two-dimensional complex cross-spectra of $|DV^R_{A-B}(\tau, t)|$ in RCP and $|DV^L_{A-B}(\tau, t)|$ in LCP. In order to avoid the cyclic convolution inherent in the Fourier transform, we expanded the functions $|DV^R_{A-B}(\tau, t)|$ and $|DV^L_{A-B}(\tau, t)|$ by zero values twice in both coordinates.

3. Results

Our results are obtained from the five one-dimensional CCF and ACF functions described at the end of the previous section. Typical examples of, for instance, the function $CCF^{LR}_{A-B}(\Delta\tau)$ for the baseline GB-WB for PSR B0823+26 and AT-HO for PSR B0833−45 (Vela) are given in Figures 1(a) and (b). The function consists of an unresolved spike and a broad component. We describe each in turn, give examples of these functions for all five pulsars, and then describe the parameter estimates.

3.1. The Unresolved Spike

Almost all of our three CCF and both of our ACF functions consist of an unresolved spike at zero delay lag, that is, at $\Delta\tau = 0$, and a smoothly and slowly varying envelope (SVE) starting at an amplitude of approximately half the amplitude of the spike and extending to several μs in negative and positive delay lags.

These characteristics are reminiscent of the ACF for pulsar microstructure, consisting of an unresolved spike at zero time lag and a broader component due to the fast intensity fluctuations of the radio emission of pulsars on the timescale of tens to hundreds of μs. These characteristics were interpreted by Rickett (1975) in terms of the amplitude-modulated noise (AMN).

Since the individual visibility functions were computed in the snapshot mode, we interpret the fine structure of $|V_{AB}(\tau)|$ in this mode to be band-limited white noise. We call it scintillation noise (SN). The amplitude of the SN is decreasing with the increasing magnitude of the time lag, Δt, in our two-dimensional ACFs, $2dACF^L(\Delta\tau, \Delta t)$ and $2dACF^R(\Delta\tau, \Delta t)$, as demonstrated in Figure 2 for the pulsar B0329+54. Such behavior can be fit by a Gaussian. Thus, we estimated the scintillation time, $t_{scint} = 115$ s, as the $1/e$ half-width of this curve. The scintillation time is in approximate agreement with the value of $t_{scint} = 110$–112 s determined earlier for this pulsar from single-dish autocorrelation spectra (Popov et al. 2017). We find the same characteristic of the SN amplitude decreasing with the increasing magnitude of the time lag, Δt, approximately as a Gaussian for each pulsar in our sample and list our values for t_{scint} in Table 1.

3.2. The Broad Component

Apart from the unresolved spike, all of our one-dimensional CCFs and ACFs are characterized by a broad component with an SVE starting at an amplitude of approximately half the amplitude of the unresolved spike at zero delay lag and extending to several μs in negative and positive delay lags. Following Popov et al.'s (2016) example of PSR B1749−28, we fit the shape of the SVE by a Lorentzian function,

$$L(\Delta\tau) = rw/(\Delta\tau^2 + w^2) + C. \qquad (1)$$

We allow for a constant, C, to compensate for a possible offset in $|DV_{A-B}(\tau, t)|$.[6] The maximum of the function above the

---

[6] In principle, the constant C should be equal to zero if the baseline of the individual visibility magnitudes, $|V_{A-B}(\tau)|$, could be exactly known and accurately subtracted. However, errors in the determinations of the baselines migrated into the construction of the dynamic visibility magnitude, $|DV_{A-B}(\tau, t)|$, and therefore into the CCFs and ACFs under consideration here. The constant, C, eliminated this influence in the fit.
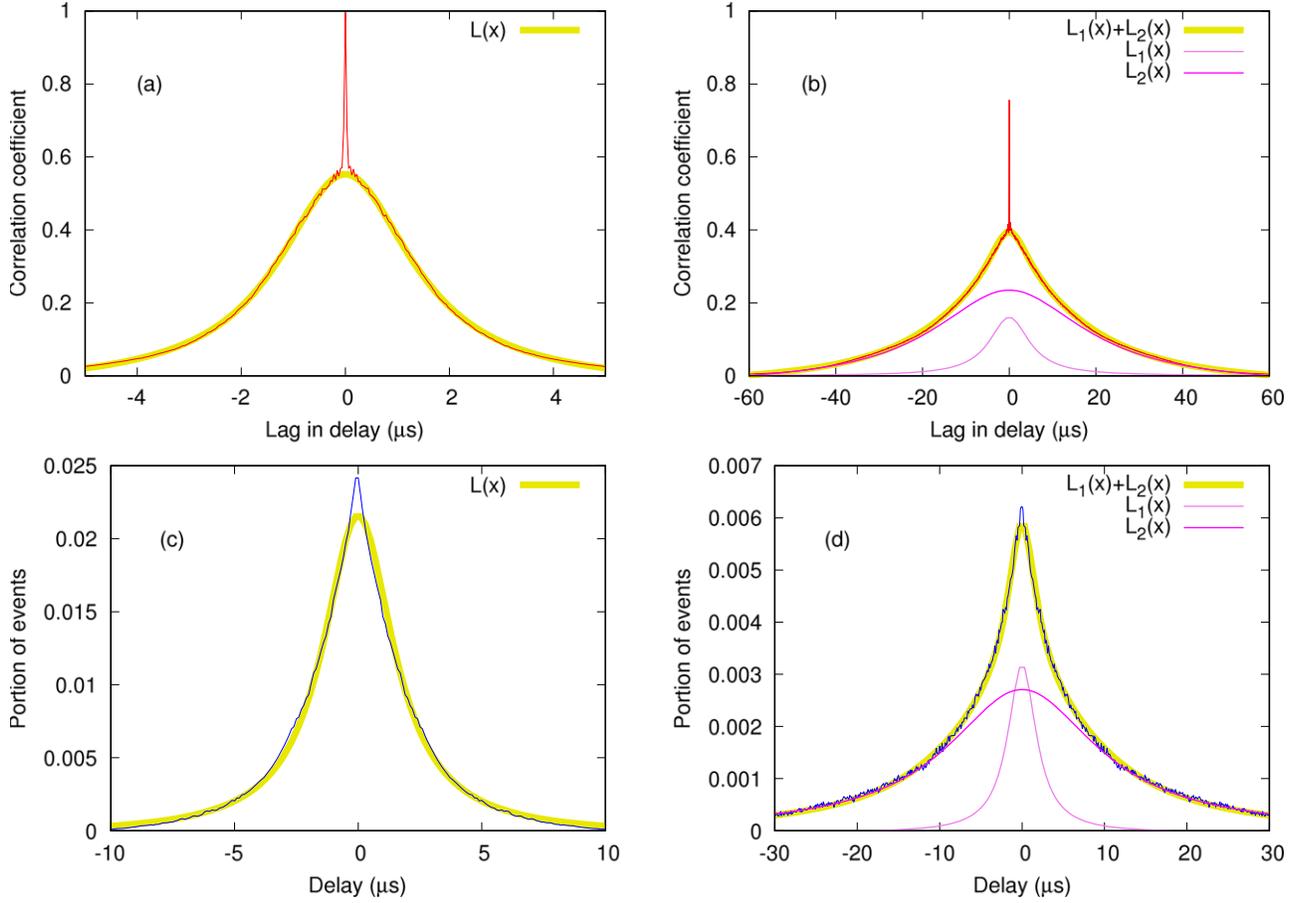
Figure 1. Upper panels: examples of the function, $\mathrm{CCF}_{A-B}^{LR}(\Delta\tau)$, for (a) PSR B0823+26 for the baseline GB-WB and (b) PSR B0833–45 (Vela) for the baseline AT-HO given in red. The best-fit Lorentzian functions outside zero lag in delay are given in yellow. For PSR B0833–45 (Vela), the best fit is a sum of two Lorentzian functions, shown as violet and magenta lines. Lower panels: results of numerical simulations of distributions of scattered rays in delay, assuming (c) a circular scattering disk and (d) an elliptical scattering disk with a 1:3 axis ratio (see Section 4 for explanation).
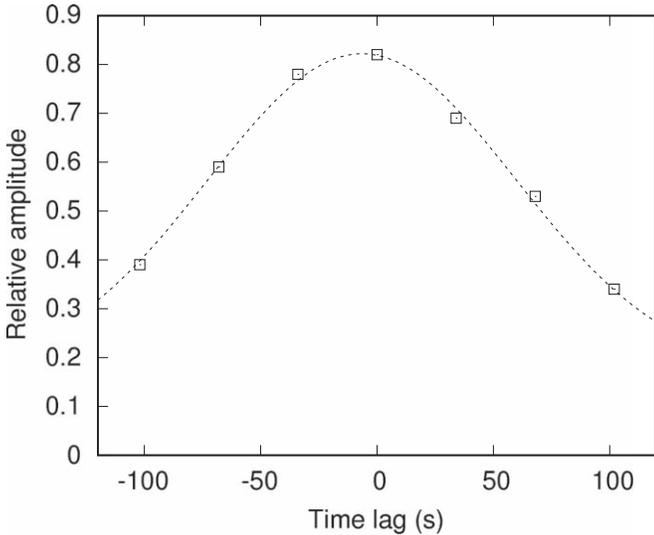

Figure 2. Relative amplitude of the unresolved spike vs. time lag, Δt, in our two-dimensional ACFs for PSR B0329+54. The dashed line corresponds to a fit with a Gaussian.

constant, C, is $A = r/w$ at $\Delta\tau = 0$, and the half-width at half-maximum (HWHM) of the function above C is w.

Temporal smearing of a pulse due to scattering in the ISM is conventionally characterized by the scattering time, $\tau_{\rm sc}$. As we

show in the Appendix, $\tau_{\rm sc} \approx w/2$ for the Lorentzians of Equation (1) fit to our CCFs and ACFs. While the determination of $\tau_{\rm sc}$ through temporal smearing of pulses is often difficult and can be prone to relatively large uncertainties, our new method of determining $\tau_{\rm sc}$ is relatively easy and can provide more accurate values. We determine the parameters through least-squares fitting. In Figure 1(a), we show the fit with a yellow line. For B0833–45 (Vela), it was obvious that a Lorentzian would not provide for a good fit. Instead, the sum of two Lorentzians with different parameters was needed. We discuss the special case of PSR B0833–45 (Vela) in more detail below. We show the fits in Figure 1(b).

3.3. Typical Examples of CCFs and ACFs for All Five Pulsars

In Figure 3, we present examples of the CCFs and ACFs and the results of the Lorentzian fits for all of the pulsars in our sample. However, instead of plotting the fit Lorentzians as in Figure 1, we plot the difference between the measured CCFs or ACFs and the fit Lorentzians to more clearly visually indicate the goodness of the fit. Furthermore, we normalize the difference by the value $L(0)$, which is shown in Figure 3 by horizontal dotted lines. The normalization permits us to directly compare the observed values of CCFs and ACFs at $\Delta\tau = 0$ with the value of $2L(0)$ predicted by the AMN model. In panels (a)–(c), (e), and (f), we show the CCFs and, in one case, the ACF for one baseline only. Assuming only a minor influence of
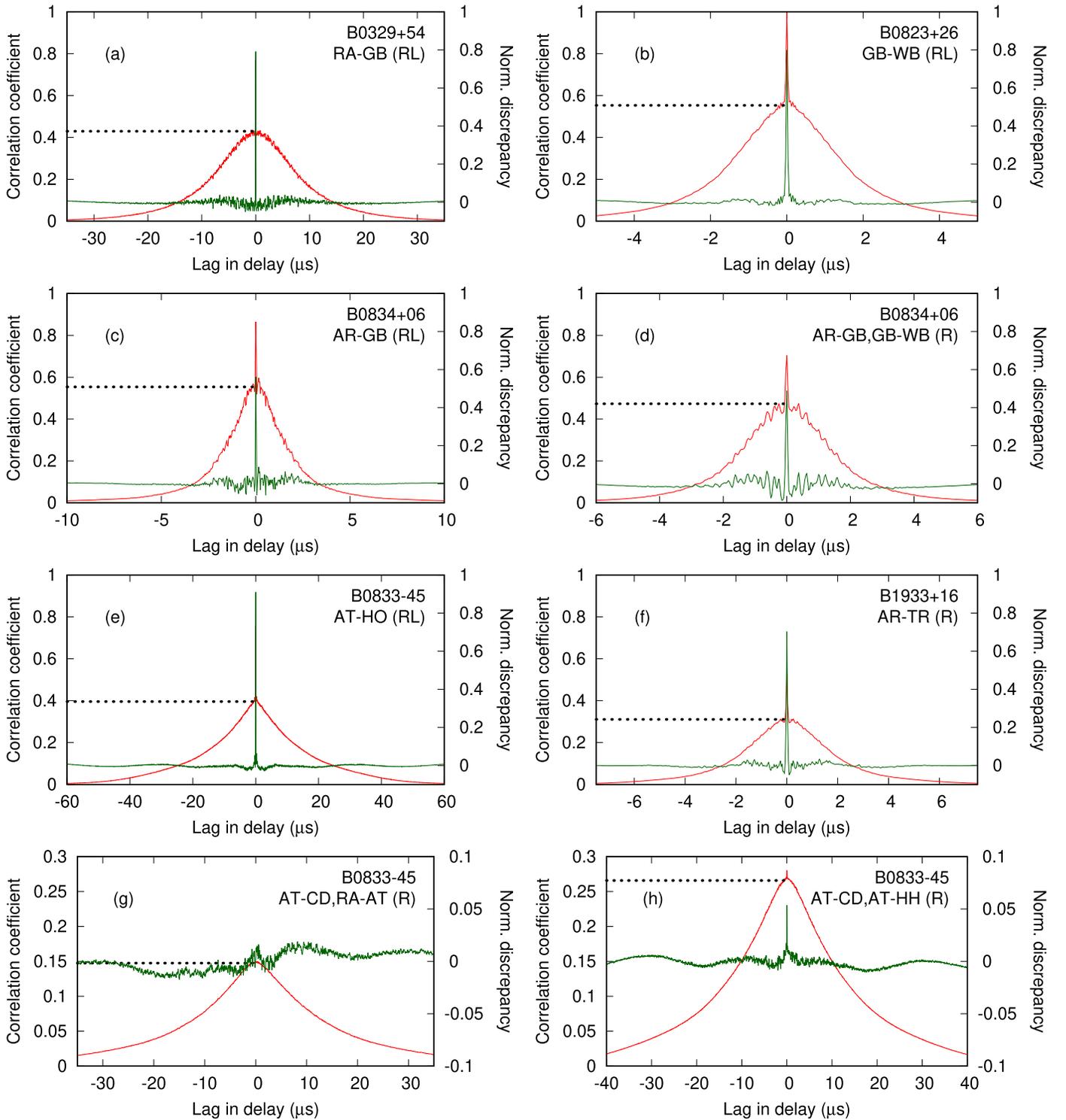
Figure 3. Examples of one-dimensional CCFs and ACFs of visibility amplitudes. Pulsar names, baselines, and polarization information are given in each panel. Observed values are plotted by red lines. Dotted lines indicate the values of $L(0)$, where $L(\Delta\tau)$ is the best Lorentzian fit of a broad smooth part of the measurements obtained outside of the narrow spike at $\Delta\tau = 0$. Green lines show the discrepancy between measured values and $L(\Delta\tau)$. The discrepancy was normalized by $L(0)$ in order to facilitate the comparison with predictions of the AMN model. For all pulsars but PSR B0833–45 (Vela), the observations are well approximated by a Lorentzian function. For Vela, the sum of two Lorentzians was needed for the fit. Note that in the two bottom panels, the scale of the vertical axis is enlarged.

cross-correlating the RCP with the LCP channel instead of autocorrelating one polarization only, these five plots should have similar characteristics concerning the unresolved spike. In panels (d), (g), and (h), we show the CCFs for two baselines. In all of our plots, for B0329+54, B0823+26, B0834+06, and B1933+16, one Lorentzian alone fits the CCFs and the ACF

well. For PSR B0833–45 (Vela), however, as already indicated in Figure 1, two Lorentzians were clearly needed.

Focusing first on the maximum of the unresolved spike, it is clear from the results for single-baseline CCFs and ACFs that the amplitude is always higher than 0.6 of the maximum of the Lorentzian, reaching 0.95, which is almost the predicted value

Table 3
Results of the Lorentzian Fits for Four Pulsars

PSR	Corr. Baselines	Function	Length ($M\lambda$)	θ_{res}/θ_{sc}	w (μs)
(1)	(2)	(3)	(4)	(5)	(6)
B0329+54	RA-GB	CCF^{LR}	65	0.66	8.0(1)
	RA-GB	CCF^{LR}	98	0.44	8.3(2)
	RA-GB	CCF^{LR}	190	0.23	8.4(1)
	RA-GB	CCF^{LR}	235	0.18	8.5(1)
B0823+26	GB-WB	CCF^{LR}	6.5	17	1.48(8)
	RA-GB	CCF^{LR}	51	2.2	0.56(6)
	RA-GB	CCF^{LR}	55	2.0	0.74(7)
	RA-GB	CCF^{LR}	61	1.8	0.87(9)
B0834+06	AR-GB	CCF^{LR}	2.5	66	1.6(1)
	AR-WB	CCF^{LR}	6.0	28	1.5(1)
	GB-WB	CCF^{LR}	6.0	28	1.5(1)
	RA-AR	CCF^{LR}	165	2.0	1.3(1)
	RA-GB	CCF^{LR}	165	2.0	1.3(2)
B1933+16	AR-TR	ACF^{R}	36	5.7	1.7(1)
	AR-SV	ACF^{R}	36	5.7	1.8(1)
	(AR-TR) × (AR-SV)	CCF^{RR}	36	5.7	1.8(2)
	RA-AR	ACF^{R}	34–164	6.0–1.2	1.5(2)

Note. Columns are as follows: (1) pulsar name; (2) two-element interferometer with stations as in Table 2; (3) the function analyzed, with $CCF^{LR} = CCF^{LR}_{A-B}(\Delta\tau)$, $ACF^{R} = ACF^{R}_{A-B}(\Delta\tau)$, and $CCF^{RR} = CCF^{R}_{(A-B)\times(C-D)}(\Delta\tau)$, with stations, A, B, C, D, as defined in Section 2; (4) length of projected baseline in millions of wavelengths, $M\lambda$; (5) interferometer angular resolution given by projected baseline length from column (4) in units of the angular scattering angle, θ_{sc}; and (6) HWHM of a Lorentzian fit to the function analyzed, where the number in parentheses is the approximate error (1σ) in the last digit of w computed from the rms variation and the number of scans during the observation time, T_{tot}, assuming Gaussian statistics.

of 1.0 for the AMN model. The situation is different for the CCFs between data from different baselines. In all three cases, the amplitude is lower than 0.6. In particular, for PSR B0833–45 (Vela), the amplitude decreases to 0.05 for the two Earth–Earth baselines and goes to zero for Earth–space to Earth–space baselines.

In contrast to the unresolved spike, for the broad component of all but PSR 0833–45 (Vela), the residuals show only very small deviations from statistical noise, indicating the excellent quality of the fit with one Lorentzian. For the broad component of B0833–45 (Vela), where two Lorentzians were needed, the residuals are somewhat larger but still indicate a good fit.

3.4. Parameter Estimates

For all of the pulsars apart from PSR B0833–45 (Vela), the results are given in Table 3. For each of the four pulsars, we list the correlated baselines as a function of increasing projected baseline length together with the corresponding interferometric angular resolution, θ_{res}, in units of the angular scattering angle, θ_{sc}, and w, the HWHM of the Lorentzian fits. A scattering disk is resolved when $\theta_{res}/\theta_{sc} < 1$.

The formal uncertainty of our estimated values for w for a single scan is about 1%–3%, while the peak-to-peak variation between successive scans is about 10%, which reflects the variation due to scintillation. The values of w are averages over the whole observing time of about 1 to a few hr and have to be

considered as obtained in the average mode of observation. There is a hint that for all pulsars but PSR B0329+54, w is decreasing with increasing baseline projection, while the scattering disk becomes more and more resolved by the beam of the two-element interferometer. Such behavior was predicted theoretically by Gwinn et al. (1998).

The anomalous dependence of w on baseline projection, $|b|$, for PSR B0329+54 can perhaps be explained by rapid changes in the properties of the scattering screen that mask the effect of the variable baseline. Observations of the pulsar by Bhat et al. (1999; Figure 4) show that at 327 MHz, the decorrelation bandwidth may change by a factor of 2 over 1 or 2 days.

It is also possible that the weak dependence of w on baseline projection for PSR B0329+54 is a consequence of the fact that the ratio θ_{res}/θ_{sc} is smaller than unity and also much lower than for other pulsars. It appears that w decreases with increasing baseline projection as long as the scattering disk is resolved, and w loses its dependence on baseline projection and becomes constant. In this context, it is interesting to note that such behavior was indeed found for the second moment of visibility by Gwinn et al. (1998). It remains to be seen whether a similar behavior can also be derived for w.

The visibility characteristics of PSR B0833–45 (Vela) are more complex; therefore, we give our results separately in Table 4. The pulsar was observed three times between 2012 and 2013, and, as in Table 3, we list the sessions and dates together with the baselines, polarization, and projected baseline lengths in order of increasing length, as well as the angular resolution in units of the scattering angle. For observing dates 2012 May 10 and 2013 December 15, we needed two Lorentzians to fit the cross sections of the CCFs and ACFs with an HWHM, w_1 and w_2, of about 4–8 μs for the short timescale and 15–25 μs for the long timescale, respectively. In contrast, for the observing date of 2012 May 18, which is about one orbit after the date of 2012 May 10, one Lorentzian was sufficient for the fit. This change is particular striking for the baseline MP-HO with the same projected baseline length and position angle but for 8 days apart. We list the values for w_1 and w_2, together with the values for the amplitudes of the Lorentzians and the position angles of the baselines, in Table 4. In contrast to B0823+26, B0834+06, and B1933+16, there is no decrease of either w_1 or w_2 with increasing projected baseline length. Further, there is also no apparent dependence of the amplitude on the baseline position angle.

We now focus on the correlation of the SN between different baseline projections in more detail. In particular, we compare the height of the unresolved spike at zero delay lag in Figures 3(d), (g), and (h). The correlation of SN between short baselines as in Figure 3(f) with projected baseline lengths of 2.5 and 6.0 $M\lambda$ is relatively high. The correlation decreases significantly between short and intermediately long baselines with lengths of 5.8–7.5 and 54 $M\lambda$ as in Figure 3(h) and completely vanishes between short and long (Earth–space) baselines of 5.8–7.5 and 630 $M\lambda$ as in Figure 3(g). These characteristics appear to be related to the size of a diffraction spot, ρ_{dif}, in the scattering screen relative to the difference of the projected lengths of the pair of the correlated baselines, B_{A-B} and B_{C-D}. If $B_{A-B} < \rho_{dif}$ and $B_{C-D} < \rho_{dif}$, then the two interferometers observe the same diffraction spot with about the same angular resolution, and consequently, for SN, the correlation is relatively high. If $B_{A-B} < \rho_{dif}$ and $B_{C-D} \sim \rho_{dif}$, the correlation decreases. In the extreme case, $B_{A-B} < \rho_{dif}$ and

Table 4
Results of the Lorentzian Fits for PSR B0833–45 (Vela)

Session	Corr. Baselines	Function	Length (Mλ)	$\theta_{\rm res}/\theta_{\rm sc}$	w_1 (μs)	w_2 (μs)	A_1	A_2	Position Angle (deg)
(1)	(2)	(3)	(4)	(5)	(6)	(7)	(8)	(9)	(10)
RAES07a	MP-PA	ACF^L	1.0	30	4.2(2)	15.5(4)	0.05	0.14	50
2012 May 10	TB-PA	ACF^L	1.5	20	5.7(6)	21.9(8)	0.12	0.31	11
	TB-HO	ACF^L	4.4	7.0	4.1(3)	16.5(8)	0.05	0.16	36
	PA-HO	ACF^L	5.8	5.2	5.0(2)	16.6(7)	0.0011	0.0012	30
	MP-HO	ACF^L	6.7	4.6	5.6(2)	18.0(2)	0.006	0.007	33
	TB-RA	ACF^L	725	0.04	12.0(4)		0.035		166
	(TB-PA) × (MP-HO)	CCF^{LL}	1.5, 6.7		5.9(2)	17.2(5)	0.024	0.035	
	(TB-PA) × (MP-PA)	CCF^{LL}	1.5, 1.0		5.9(1)	19.2(5)	0.089	0.187	
	(TB-PA) × (MP-TB)	CCF^{LL}	1.5, 2.4		6.3(2)	23.2(6)	0.14	0.32	
	(TB-RA) × (MP-TB)	CCF^{LL}	725, 2.4		6.4(2)	17.4(4)	0.032	0.090	
RAES07b	AT-MP	CCF^{LR}	0.5	61	17.1(4)		0.32		45
2012 May 18	PA-MP	CCF^{LR}	1.0	30	18.0(4)		0.39		50
	PA-AT	CCF^{LR}	1.5	20	20.5(5)		0.44		45
	PA-HO	CCF^{LR}	5.8	5.2	13.8(4)		0.14		30
	MP-HO	CCF^{LR}	6.7	4.6	11.4(4)		0.004		33
	AT-HO	CCF^{LR}	7.3	4.3	12.4(3)		0.08		33
	AT-HH	CCF^{LR}	52.2	0.58	19.6(5)		0.04		90
	AT-RA	CCF^{LR}	1065	0.03	14.0(3)		0.017		166
	(PA-AT) × (AT-MP)	CCF^{RR}	1.5, 0.5		18.8(4)		0.39		
	(AT-HH) × (PA-HH)	CCF^{RR}	52.2, 52.2		20.1(5)		0.43		
RAKS02as	AT-CD	CCF^{LR}	5.8–7.5	5.2–4.1	5.0(2)	15.9(3)	0.22	0.30	112–150
2013 Dec 15	AT-HO	CCF^{LR}	6.6–7.3	4.6–4.3	4.4(1)	19.7(3)	0.14	0.28	33-46
	AT-HH	CCF^{LR}	54	0.55	7.8(1)	22.0(4)	0.15	0.26	80–92
	AT-RA	CCF^{LR}	630	0.05	8.6(2)	25.0(4)	0.08	0.06	130
	(AT-CD) × (HO-CD)	CCF^{RR}	5.8–7.5, 9.3		1.1(1)	10.0(2)	0.03	0.05	
	(AT-CD) × (AT-HO)	CCF^{RR}	5.8–7.5, 6.6–7.3		3.3(1)	17.4(3)	0.20	0.10	
	(AT-CD) × (AT-RA)	CCF^{RR}	5.8–7.5, 630		6.0(2)	17.9(3)	0.06	0.09	
	(AT-CD) × (AT-HH)	CCF^{RR}	5.8–7.5, 54		6.6(2)	19.3(4)	0.11	0.17	
	(AT-HH) × (AT-RA)	CCF^{RR}	54, 630		7.3(2)	18.3(4)	0.07	0.10	

Note. Columns are as follows: (1) session code and date; (2) designation of baseline or baseline combination; (3) function analyzed (for definition, see Table 3); (4) length of baseline projection in millions of wavelengths, Mλ; (5) interferometer angular resolution given by projected baseline length from column (4) in units of the angular scattering angle, $\theta_{\rm sc}$; (6) and (7) HWHM of a Lorentzian fit of the function in column (3), where in the majority of cases, a sum of two Lorentzians with HWHM w_1 for the narrow Lorentzian and HWHM w_2 for the broad Lorentzian was needed to fit the shape of the SVE, and errors in parentheses are defined as in Table 3; (8) and (9) amplitudes corresponding to Lorentzians with w_1 and w_2, respectively; (10) position angle of baseline projection in degrees.

$B_{C-D} > \rho_{\rm dif}$, the correlation completely vanishes, since the two interferometers observe different diffraction spots.

4. Numerical Simulation of Scattering

Our analysis of the CCFs and ACFs has shown that for the set of our pulsars, a single Lorentzian was sufficient for the fit, except for B0833–45 (Vela), for which in many cases the sum of two Lorentzians was needed. Through a numerical simulation, we show that the difference can be interpreted in terms of circularly and noncircularly symmetric scattering of the radio radiation in the inhomogeneities of the scattering screen.

We consider the probability distribution in delay for scattered rays refracted on a thin screen. For the small angle approximation, the geometric time delay, τ, is given as a function of the scattering angle, θ, as $\tau = \theta^2 d_{\rm eff}/(2c)$, where $d_{\rm eff} = Dd/(D-d)$, with D and d as distances to the pulsar and the screen, respectively (Gwinn et al. 1993). Let the screen contain n refractors with coordinates x_i, y_i ($1 \leqslant i \leqslant n$), selected from a two-dimensional Gaussian distribution with standard deviations corresponding to major and minor axes equal to σ_x^2 and σ_y^2, respectively. We compute the mutual geometrical

delays between each of the rays as $\tau_{ij} = \theta_i^2 - \theta_j^2$ with $n(n-1)$ combinations. Since $\theta^2 \propto \rho^2 = x^2 + y^2$, we compute the delays as $\tau_{ij} = \rho_i^2 - \rho_j^2$. In order to achieve a smooth distribution, we assume $n = 100$, and we average 100 simulations.

In Figure 1(c), we show the distribution of computed delays for a circular ($\sigma_x = \sigma_y$) scattering disk, and in Figure 1(d), we show them for an elliptical scattering disk ($\sigma_y = 3\sigma_x$). For the circular disk, the distribution is well fit by a single Lorentzian, whereas for the elliptical disk, the sum of two Lorentzians is needed. The distributions shown in Figures 1(c) and (d) reflect the shape of the average visibility function in delay. As explained in the Appendix, the ACF of a Lorentzian is also a Lorentzian, with an HWHM twice as large as that of the original Lorentzian. Similarly, for our cases, the CCFs of the Lorentzians we consider are also, at least approximately, Lorentzians, although that is harder to show, as explained in the Appendix. Despite the simplicity of our model, we found a good correspondence between the simulated distributions and the SVEs of the CCFs and ACFs obtained in our analysis of the substructure of visibility functions for pulsars. Our analysis is valid for an interferometer with a short baseline when a

scattering disk is not resolved. The scale of the time delay in the bottom panels of Figure 1 is arbitrary; it depends on the values of the distance to the pulsar D, the distance to the screen d, and the scattering angle θ.

5. Discussion

The main result of our analysis is that Lorentzians fit the SVE in our CCFs and ACFs—therefore, in general, the envelope of the two-element interferometer delay visibility functions very well—and numerical simulations of scattering confirm that Lorentzians are indeed expected. Isotropic scattering in the plane of the sky results in a single Lorentzian for the SVE of the CCFs and ACFs with an HWHM twice as large as τ_{sc}, whereas anisotropic scattering with the scattering disk being elliptical results in two Lorentzians with different HWHMs. In fact, since we found that Lorentzians can be fit for all five pulsars with a variety of pulsar parameters, it is likely that this is a general characteristic of all pulsars that the delay visibility functions can be described by one or possibly more Lorentzians, depending on the complexity of the scattering medium. Our pulsars B0329+54, B0823+26, B0834+06, and B1933+16 are all undergoing isotropic scattering. Their galactic coordinates and the relative distances of their scattering screens (see Table 1) indicate that, for the first three pulsars, the screens are approximately associated with the Local Arm in our Galaxy, and, for B1933+16, they are associated with the Carina Sagittarius Arm (see also Popov et al. 2017; Fadeev et al. 2018). Despite the large range of their distances, D; dispersion measures, DM; scintillation times, t_{scint}; scattering times, τ_{sc}; scattering angles, θ_{sc}; and decorrelation bandwidths, Δf_{dif}, no dependence on any of these parameters can be found in the quality of the fit apart from only slight differences in the small deviations from a noise-like distribution of the residuals.

In contrast, PSR B0833–45 (Vela) shows more complex behavior. Only one set of our data can be satisfactorily fitted with a single Lorentzian, while a data set taken 8 days earlier and another data set taken 7 months later require a sum of two Lorentzian functions with different widths, w_1 and w_2.

It is particularly striking that for the same baseline, MP-HO, with the same projected length and position angle, on 2012 May 10, two Lorentzians are needed for the fit, and on 2012 May 18, only one Lorentzian is needed. Apparently, the scattering conditions for this pulsar changed drastically over a time span as short as 1 week. Anisotropic scattering, indicated by the two Lorentzians, changed to isotropic scattering, indicated by the one Lorentzian, and then back to anisotropic scattering.

Earlier, Popov et al. (2019) had already found evidence of anisotropic scattering for this pulsar by comparing the dependence of visibility amplitude on baseline projection at different baseline position angles. Our method described in this paper is largely independent of that method and has advantages with respect to higher signal-to-noise ratios and more robust estimates of scattering characteristics.

That properties of an intervening medium on the line of sight to PSR B0833–55 (Vela) differ qualitatively from properties of such media for the other four pulsars can be understood because of the peculiarities of PSR B0833–55 (Vela). The Vela pulsar has the largest mean free electron density along the line of sight; the smallest values of t_{scint} and, together with B0329+54, Δf_{dif}; and the largest values of τ_{sc} and θ_{sc}. The pulsar is the only one of our sample that is still within a visible supernova remnant.

Popov et al. (2019) argued on the basis of the determination of the scattering medium position that scintillations of PSR B0833–55 (Vela) originate at least partly within the supernova remnant. The regions responsible for the scattering there differ significantly from the standard model of a thin screen. In particular, the line of sight is likely to be nearly tangent to the scattering sheets, which are expected to be highly turbulent and rapidly moving. It is therefore conceivable that the scattering screen parameters are highly variable, even on such a short timescale of 1 week. In this model, the anisotropic indicatrix and rapid variability of the scattering screen parameters are produced naturally.

6. Conclusions

We present an analysis of two-element interferometry data with Earth–Earth and Earth–space baselines for five pulsars: B0329+54, B0823+26, B0834+06, B1933+16, and B0833–45 (Vela), the latter still embedded in its supernova remnant. The cross-correlation and ACFs of the interferometer dynamic visibility functions in delay and time consist of a band-limited unresolved spike at zero delay lag in $\Delta\tau$ and zero time lag in Δt, interpreted as being due to SN and a smooth SVE. The amplitude of the SN spike above the SVE is between 0.6 and 0.95 times the amplitude of the SVE, which is reminiscent of the AMN model for pulsar microstructure. The amplitude of the SN spike decreases with Δt on a timescale corresponding to the scintillation time, t_{scint}. The SN for baseline projections smaller than the size of the diffraction spot, ρ_{dif}, is uncorrelated with the SN for baseline projections larger than ρ_{dif}. The SVEs in delay lag, supported by numerical simulations, show that they are well approximated by one or more Lorentzian functions. For all pulsars but B0833–45 (Vela), only a single Lorentzian was needed for the fit, indicating isotropic scattering by a thin screen. For B0833–45 (Vela), usually at least two Lorentzians with variable widths were needed for the fit, indicating anisotropic scattering, likely in the shell of the supernova remnant and/or the Gum Nebula, with scattering conditions variable on a timescale of 1 week or less.

It is likely that the SVEs of all pulsars can be described by one or more Lorentzians, depending on the complexity of the intermittent scattering material of the ISM, and that fit Lorentzians are a new and more robust way to describe some scattering properties.

Appendix
Scattering Time Expressed through the Scale Parameter of a Lorentzian Fit of a Correlation Function

In this Appendix we obtain the equation $\tau_{\text{sc}} = w/2$ used in Section 3.2. The derivation is based on the assumption that the observed intrapulse variations of fringe visibility magnitude can be described by the AMN model developed by Rickett (1975). In order to make the relationship with the AMN model clear, the notations chosen here are close to those used in the cited paper. In particular, for a fixed baseline A–B and polarization P ($P = L$ or $P = R$), we designate $I(\tau) = |V^P_{A-B}(\tau)|$. The functions $\text{ACF}^P_{A-B}(\Delta\tau)$, introduced in Section 2 may be expressed as $\text{ACF}^P_{A-B}(\Delta\tau) = \langle R_I(\Delta\tau)\rangle$, where $\langle \ \rangle$ denotes the ensemble average, and the operator, R, acting on a random process $z(\tau)$, is defined by

$$R_z(\Delta\tau) = \int z(\tau)z(\tau + \Delta\tau)d\tau, \qquad (2)$$

with integration performed over the total duration of the pulse. Further, we decompose the observed variability of the visibility magnitude as $I(\tau) = a^2(\tau)I_1(\tau)$. Here, $a^2(\tau)$ is a deterministic, slowly varying function that reflects the time dependence of $\langle I(\tau)\rangle$. The factor $I_1(\tau)$ is a stationary random process describing the SN that originates in the scattering matter. The timescale of SN variations is much smaller than the timescale of variations of the modulating function.

If we additionally assume that there exists such a stationary complex Gaussian random process, $x(\tau)$, that

$$I_1(\tau) \approx |x(\tau)|^2, \qquad (3)$$

then the AMN model is directly applicable to our problem. The important consequence of the model is that $\langle R_I(\Delta\tau)\rangle = R_I^{\text{b}}(\Delta\tau) + R_I^{\text{c}}(\Delta\tau)$. Here the term R_I^{b} is the broad component that varies slowly over the whole range of $\Delta\tau$, and the term R_I^{c} represents the narrow central spike with

$$R_I^{\text{b}}(\Delta\tau) \propto R_{a^2}(\Delta\tau), \qquad (4)$$

$$R_I^{\text{c}}(0) = R_I^{\text{b}}(0). \qquad (5)$$

The values $R_I^{\text{c}}(0)$ and $R_I^{\text{b}}(0)$ can be easily measured observationally. If Equation (5) is satisfied with sufficient precision, then it is likely that the AMN model is applicable, Equation (4) also holds, and the determination of the modulating function, $a^2(\Delta\tau)$, reduces to the problem of finding a function with the given autocorrelation.

For CCFs, it is difficult, if possible at all, to find a complete analog to the function $I(\tau)$. Thus, the line of reasoning based

on direct use of the results of Rickett (1975) is not applicable. But the overall similarity of the mathematics encountered in considering both the ACFs and CCFs (in all cases, we analyze mixed fourth moments of the incident field) makes it likely that if Equation (5) is satisfied with sufficient precision, then Equation (4) can be used to determine the form of the modulating function.

In finding $a^2(\Delta\tau)$, we use for the broad component $R_I^{\text{b}}(\Delta\tau)$ of the measured function $\langle R_I(\Delta\tau)\rangle$ the approximation

$$R_I^{\text{b}}(\Delta\tau) = L(\Delta\tau, w, C), \qquad (6)$$

where $L(\Delta\tau, w, C) = rw/(\Delta\tau^2 + w^2) + C$. We assume that the constant offset, C, is caused only by errors in the determination of baselines of the individual visibility magnitudes, that is, $C = 0$ in Equation (6). Using the identity $R_{L(\Delta\tau,y,0)} = rpL(\Delta\tau, 2y, 0)$, where the operator, R, is defined in Equation (2), we obtain from Equation (4) that $\tau_{\text{sc}} = w/2$, where the scattering time, τ_{sc}, is defined as the HWHM of $a^2(\Delta\tau)$.

ORCID iDs

M. V. Popov ⓘ https://orcid.org/0000-0001-7931-646X
M. S. Burgin ⓘ https://orcid.org/0000-0002-0579-2938
C. R. Gwinn ⓘ https://orcid.org/0000-0002-6936-4430

References

Bhat, N. D. R., Rao, A. P., & Gupta, Y. 1999, ApJS, 121, 483
Fadeev, E. N., Andrianov, A. S., Burgin, M. S., et al. 2018, MNRAS, 480, 4199
Goodman, J., & Narayan, R. 1989, MNRAS, 238, 995
Gwinn, C. R., Bartel, N., & Cordes, J. M. 1993, ApJ, 410, 673
Gwinn, C. R., Britton, M. C., Reynolds, J. E., et al. 1998, ApJ, 505, 928
Gwinn, C. R., Popov, M. V., Bartel, N., et al. 2016, ApJ, 822, 96
Johnson, M. D. 2016, ApJ, 833, 74
Johnson, M. D., & Gwinn, C. R. 2015, ApJ, 805, 180
Johnson, M. D., & Narayan, R. 2016, ApJ, 826, 170
Kardashev, N. S., Khartov, V. V., Abramov, V. V., et al. 2013, ARep, 57, 153
Likhachev, S. F., Kostenko, V. I., Girin, I. A., et al. 2017, JAI, 6, 1750004
Narayan, R., & Goodman, J. 1989, MNRAS, 238, 963
Pence, W. 1999, in ASP Conf. Ser. 172, Astronomical Data Analysis Software and Systems VIII, ed. D. M. Mehringer, R. L. Plante, & D. A. Roberts (San Francisco, CA: ASP), 487
Popov, M. V., Andrianov, A. S., Bartel, N., et al. 2016, ARep, 60, 792
Popov, M. V., Andrianov, A. S., Burgin, M. S., et al. 2019, ARep, 63, 391
Popov, M. V., Bartel, N., Gwinn, C. R., et al. 2017, MNRAS, 465, 978
Prokhorov, A., Bunkin, V. F., Gochelashvily, K. S., & Shishov, V. I. 1975, IEEEP, 63, 790
Rickett, B. J. 1975, ApJ, 197, 185
Rickett, B. J. 1977, ARA&A, 15, 479
Shishov, V. I., Smirnova, T. V., Sieber, W., et al. 2003, A&A, 404, 557